

Geophysical Research Letters

RESEARCH LETTER

10.1029/2019GL083588

Key Points:

- Patterns in the stratigraphy of Mars' south polar ice sheet are consistent with orbital climate forcing
- Mars' south polar ice sheet accumulated nonuniformly at rates of 0.11–0.39 mm/year
- Similar orbital oscillations forced the accumulation of the northern and southern ice sheets

Supporting Information:

- Supporting Information S1
- Data Set S1

Correspondence to:

P. Becerra,
patricio.becerra@space.unibe.ch

Citation:

Becerra, P., Sori, M. M., Thomas, N., Pommerol, A., Simioni, E., Sutton, S. S., et al (2019). Timescales of the climate record in the south polar ice cap of Mars. *Geophysical Research Letters*, 46, 7268–7277. <https://doi.org/10.1029/2019GL083588>

Received 3 MAY 2019

Accepted 18 JUN 2019

Accepted article online 24 JUN 2019

Published online 5 JUL 2019

Timescales of the Climate Record in the South Polar Ice Cap of Mars

Patricio Becerra¹ , Michael M. Sori² , Nicolas Thomas¹ , Antoine Pommerol¹, Emanuele Simioni³ , Sarah S. Sutton² , Stepan Tulyakov⁴, and Gabriele Cremonese³

¹Physikalisches Institut, Universität Bern, Bern, Switzerland, ²Lunar and Planetary Laboratory, University of Arizona, Tucson, AZ, USA, ³Istituto Nazionale di Astrofisica, Osservatorio Astronomico di Padova, Padova, Italy, ⁴Ecole Polytechnique Fédérale de Lausanne, Lausanne, Switzerland

Abstract The South Polar Layered Deposits (SPLD) are the largest water ice reservoirs on Mars. Their accumulation is believed to result from climate oscillations that drive the movement of ice and dust on the surface. The High-Resolution Imaging Science Experiment and the Colour and Stereo Surface Imaging System have imaged exposures of its internal structure in troughs and marginal scarps. Here we use the stereo imaging products of these instruments to extract stratigraphic profiles representative of various locations throughout the SPLD. Through wavelet and series-matching analyses of these profiles, we reveal periodicities in the stratigraphy that correlate to the orbital oscillations that drive climate change on Mars and that have been observed to force the accumulation of the north polar cap. We infer that the water ice and dust of the SPLD were deposited at variable rates of 0.13–0.39 mm/year, taking a minimum of 10–30 Myr to accumulate.

Plain Language Summary The single location on Mars with the most water ice is in the southern polar ice cap, in the so-called South Polar Layered Deposits (SPLD). Changes in Martian climate through time affect the locations on Mars where ice is stable, and it is believed that these changes drove the accumulation of layers upon layers of ice and dust in the SPLD. The High-Resolution Imaging Science Experiment and the Colour and Stereo Surface Imaging System are satellite cameras that have photographed troughs and scarps within the SPLD to produce 3-D views of this layered internal structure. We analyzed this structure and found patterns in the layering related to variations of Mars' orbit and spin axis. These variations drive climate change on Mars, so our analysis confirms the connection between the SPLD and Mars' astronomical parameters. From this relationship, we inferred that the ice and dust of the SPLD took at least 10–30 Myr to accumulate.

1. Introduction and Background

The polar layered deposits (PLD) of Mars compose most of the Martian polar ice caps. Their stratified structure of ice and dust (Figure 1), visible remotely in scarps and spiral troughs (Cutts et al., 1976), has been hypothesized to contain a decipherable record of climate (Cutts, 1973; Murray et al., 1973) resulting from oscillations in Mars' astronomical parameters (Cutts & Lewis, 1982; Howard et al., 1982; Laskar et al., 2002; Murray et al., 1973; Toon et al., 1980), analogous to Milankovitch cycles recorded in Earth's geologic record (Hays et al., 1976). One of the main objectives of Mars polar science is to connect patterns in the PLD structure to patterns in these oscillations, to effectively “read” the Martian climate record (Smith et al., 2017).

Observations of the North PLD (NPLD) by orbital imagers (Becerra et al., 2017; Fishbaugh et al., 2010; Fishbaugh & Hvidberg, 2006; Laskar et al., 2002; Limaye et al., 2012; Milkovich, 2005) and subsurface sounding radar (Lalich & Holt, 2017; Phillips et al., 2008; Putzig et al., 2009; Smith et al., 2016), as well as models of its accumulation (Hvidberg et al., 2012; Levard et al., 2007), generally support the theory that the stratigraphic record of the NPLD is forced by orbital oscillations. No such conclusions have been made for the South PLD (SPLD, Figure 1a). One reason for this is the difference in surface age between both PLD: The latest NPLD estimate is 0–1,500 years (Brown et al., 2016; Landis et al., 2016), whereas SPLD estimates vary regionally between 7–14 Myr (Herkenhoff, 2000) and 30–100 Myr (Koutnik et al., 2002). As the solutions for the past orbital evolution of Mars are nonunique before ~20 Ma (Laskar et al., 2004), there is

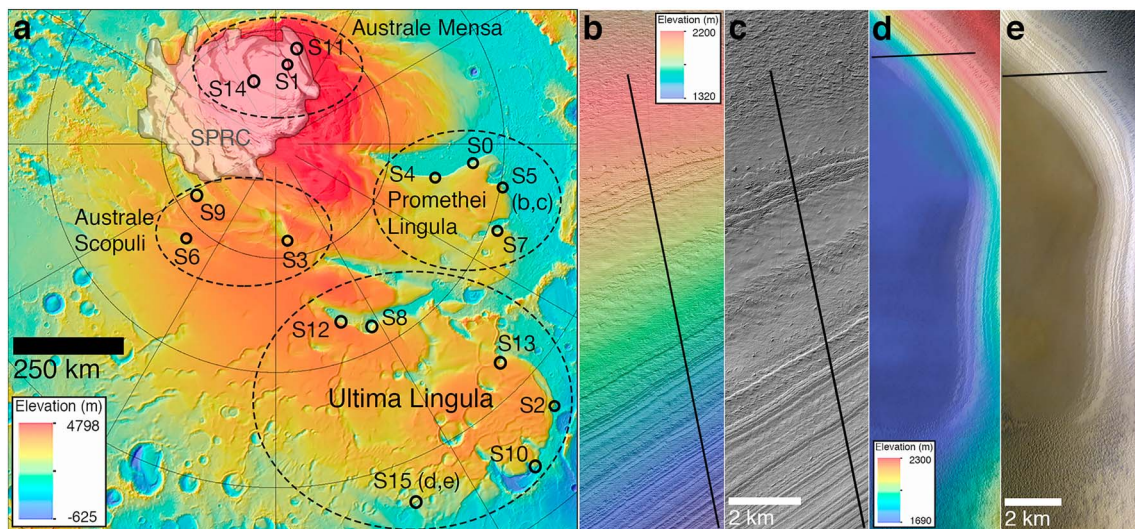


Figure 1. (a) Topographic colored relief map (Mars Orbiter Laser Altimeter) of the South Polar Layered Deposits with study site locations and their grouping. (b) Colored relief view of the High-Resolution Imaging Science Experiment digital terrain model of site S5. In (b), (c), (d), and (e) black lines trace the ground track of the extracted profiles. (c) High-Resolution Imaging Science Experiment orthorectified image of site S5 displaying the exposed bedding. (d) Colored relief view of Colour and Stereo Surface Imaging System digital terrain model in site S15. (e) Colour and Stereo Surface Imaging System full color image composed with the RED, PAN, and BLU filters.

no reliable climate function to compare to the SPLD record, which has discouraged prospects of tying the SPLD to astronomical forcing.

Analyses of the SPLD using images, topography, and radar have identified different stratigraphic units. A three-sequence, large-scale stratigraphy (Milkovich & Plaut, 2008; the bench-forming layer [BFL] sequence (Byrne & Ivanov, 2004), the Promethei Lingula layer [PLL] sequence, and the inferred layer sequence) was the starting point for future stratigraphic mapping. Posterior measurements of bed thickness and slope trends showed no signs of orbital forcing (Limaye et al., 2012), but the identification of a widespread recent accumulation package (WRAP) in both PLD by the Shallow Radar (Seu et al., 2007) allowed dating of the beds above this WRAP to ~370 ka based on ice-deposition modeling of the NPLD (Smith et al., 2016). Recently, a radar-based SPLD structure with three facies was described and correlated to previously mapped units (Whitten & Campbell, 2018). Still, no signs of orbital forcing that could enable estimates of accumulation timescales have been discovered in the SPLD water ice units.

Here we measure periodicities in SPLD bedding exposures and compare them to the characteristic frequencies of Mars' insolation to test for astronomical forcing. We use digital terrain models (DTMs) of SPLD outcrops made from stereo images taken by the High-Resolution Imaging Science Experiment (HiRISE (McEwen et al., 2007)), along with the first DTM of the SPLD produced by the Colour and Stereo Surface Imaging System (CaSSIS (Thomas et al., 2017)). We investigate discrepancies in the signals that may discriminate between different epochs of accumulation, and we estimate accumulation rates. In addition, we compare the detected signals and stratigraphic profiles of the SPLD to those of the NPLD, to investigate the relationship between Mars' polar caps.

2. Data and Methods

Our data set (Figure 1a and supporting information Table S1) consists of 15 HiRISE DTMs (e.g., Figures 1b and 1c; Kirk et al., 2008) and one CaSSIS DTM (Figure 1d) of exposed SPLD beds. The CaSSIS stereo image pair was taken within one orbit of the host spacecraft - the ExoMars Trace Gas Orbiter (TGO) (Thomas et al., 2017) - resulting in both images having the same lighting and surface conditions. The CaSSIS DTM was produced using the 3DPD pipeline (Simioni et al., 2017; see supporting information).

2.1. Stratigraphic Profiles

To observe periodic signals in the stratigraphy connected to orbitally forced accumulation of the SPLD, we require depth profiles from the outcrops that represent physical properties of the internal beds. These profiles must act as “virtual ice cores” of the Martian ice sheets, showing the change with depth of a particular property of the SPLD. In the NPLD, the “protrusion” of exposed beds relative to the average slope of the trough wall was shown to be a proxy for resistance to erosion (Becerra et al., 2016) and is more likely to have a direct relationship to internal properties of the strata than to the brightness of the exposure (Herkenhoff et al., 2007). This distinction may be especially important for the SPLD, given that outcrop brightness is more uniform with depth than in the NPLD (Limaye et al., 2012; Milkovich, 2005; Milkovich & Plaut, 2008) and thus more likely to represent a noninternal layer property, like sublimation lag or postexposure deposited dust.

We extracted depth-varying protrusion profiles from 16 study sites (Figure 1a) by fitting a line within a localized window along a 1-D topographic profile in the DTM and measuring the normal distance between the topography and the linear fit at the center of the window. This difference is the protrusion at each point of the profile. A depth-dependent protrusion profile is then obtained by moving the window and calculating this difference along the entire topographic track. This method is similar to that of Becerra et al. (2016). We selected a window size of 350 m, the same used for the NPLD, and averaged five parallel profiles spaced 10 m apart to reduce noise caused by local roughness (Becerra et al., 2016). Figure 2a shows the average protrusion profile for site S5 (details of the procedure are given in Figure S1). All 16 profiles are in Figure S2.

2.2. Depth-Series Analysis

The search for periodicities in the protrusion profiles uses wavelet analysis (Torrence & Compo, 1998). A wavelet transform decomposes one-dimensional time series (here time is represented by depth) into their components in time-frequency (depth-wavelength) space (Becerra et al., 2017). The wavelet transform of each profile is computed by normalizing the profiles to zero mean and unit variance and then convolving with the selected wavelet function (see supporting information). The wavelet power spectrum (WPS) is the square of the real part of the transform and shows the change in power with wavelength and depth (Becerra et al., 2017; Torrence & Compo, 1998). In the WPS, the abscissa of peaks in power represent dominant wavelengths in the profile (e.g., Figure 2b).

However, we must account for the probability that a randomly generated profile could have similar periodicities with high power. The statistical significance of periodicities in paleoclimate records can be constrained by assuming that the record is modulated by red noise (first-order autoregressive process “AR(1)”) and comparing the spectral power of the records to that of random simulations of this background (Mann & Lees, 1996). Stratigraphic records of the Martian NPLD follow an AR(1) background (Becerra et al., 2017; Perron & Huybers, 2009), and we show this to also apply to the SPLD (Figure S3). Thus, we tested for significance of the detected wavelengths in each study site by comparing the WPS of the protrusion profiles to that of an AR(1) background. For each profile, we simulated 10,000 AR(1) series with the same mean and variance as the profile and compared their wavelet power at every point in wavelength-depth space. We then drew contours of confidence in the WPS of the real profile that delineate regions of this space in which the power of the profile is higher than 95% of the simulations (e.g., Figure 2b), following previous work and convention (Becerra et al., 2017; Perron & Huybers, 2009; Torrence & Compo, 1998).

To ensure selection of only the most dominant periodicities in the profiles, we required that the measured wavelengths be statistically valid for at least 5 times the wavelength value (i.e., a 20-m wavelength must be valid for ≥ 100 m) and for $>20\%$ of the total depth of the profile. The comparison with the orbital forcing function considers only those profiles with two overlapping wavelengths (Figure 2d and Table S2). In periodic sequences such as the PLD, the detection of one dominant wavelength does not imply forcing. Rather, detections of pairs of periodicities with a characteristic ratio similar to the ratio between orbital oscillation frequencies can be used as evidence for this forcing and to estimate time-averaged accumulation rates and timescales (Becerra et al., 2017; Lewis & Aharonson, 2014; Lewis et al., 2008).

2.3. Profile Comparison

In addition to testing for orbital forcing, we use the measured periodicities to compare each study site and estimate relationships between records in different geographic and stratigraphic positions. We

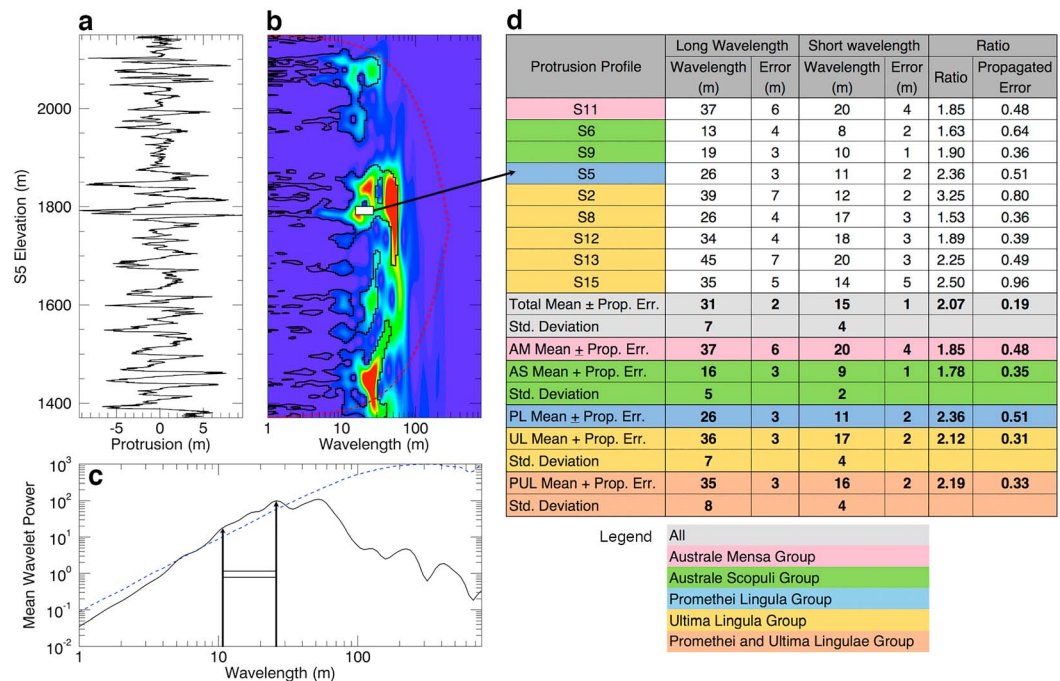


Figure 2. (a) Protrusion profile of site S5. (b) Wavelet power spectrum of S5. Warmer colors signify higher power, and black curves delineate the 95% confidence contours over red noise, within which periodicities have statistically significant power. The red dashed line marks the cone of influence in the wavelet power spectrum, outside which peaks in power are unreliable (Torrence & Compo, 1998). The white bar represents the S5 wavelength ratio of 2.36. (c) Global wavelet spectrum of S5. The blue dashed line is the 95% confidence level over red noise. Vertical arrows denote the two dominant wavelengths identified based on the criteria explained in the text, with the white bar representing the same ratio as in (b). (d) Table with wavelet analysis results for all sites. Colors represent the different geographic groups. AM = Australe Mensa; AS = Australe Scopuli; PL = Promethei Lingula; PUL = Ultima Lingula; UL = Ultima Lingula.

hypothesize that profiles extracted from previously mapped stratigraphic units will have similar wavelengths and conform a single record that may be separate from a record in another unit with different wavelengths.

We complement this correlation with dynamic time warping (DTW), a signal-matching algorithm previously used to compare profiles of real and simulated stratigraphy in the NPLD (Becerra et al., 2016; Sori et al., 2014). DTW tunes a stratigraphic profile to search for the optimal match between it and another profile that is kept fixed (see supporting information text and Figure S4).

DTW is also used to compare the SPLD profiles to NPLD profiles (Becerra et al., 2016, 2017). However, given the age difference between both PLD, and as DTW does not uniquely prove one signal is forced by another (Becerra et al., 2016), we do not assume that a good match here implies that both profiles represent the same record but rather that they have a high probability of having been influenced by the same forcing functions.

3. Results

3.1. Wavelet Analysis

We grouped the study sites based on their stratigraphic and geographic location (Figure 1a). Figures 2a–2c show how dominant wavelengths were measured in site S5 (WPS of all 16 sites are in Figure S2). To compare pairs of periodicities (Becerra et al., 2017; Lewis et al., 2008), we measured a long and a short dominant wavelength in all profiles where it was possible and calculated the mean and standard deviation of each in every group. The ratio of long/short mean wavelengths in each group is the representative candidate “climate signal” for that group. These measurements are shown in Figure 2d for all sites and groups. Uncertainties of the measured wavelengths are in general the half width at half maximum of the peak in global (i.e., depth averaged) wavelet power at that wavelength (Figure 2c), but we also assumed a systematic error of measured wavelengths equal to at most the upper limit vertical precision of the DTMs (≤ 2 m for HiRISE, ≤ 5 m for CaSSIS). Uncertainties for the means are the propagated uncertainties within each group.

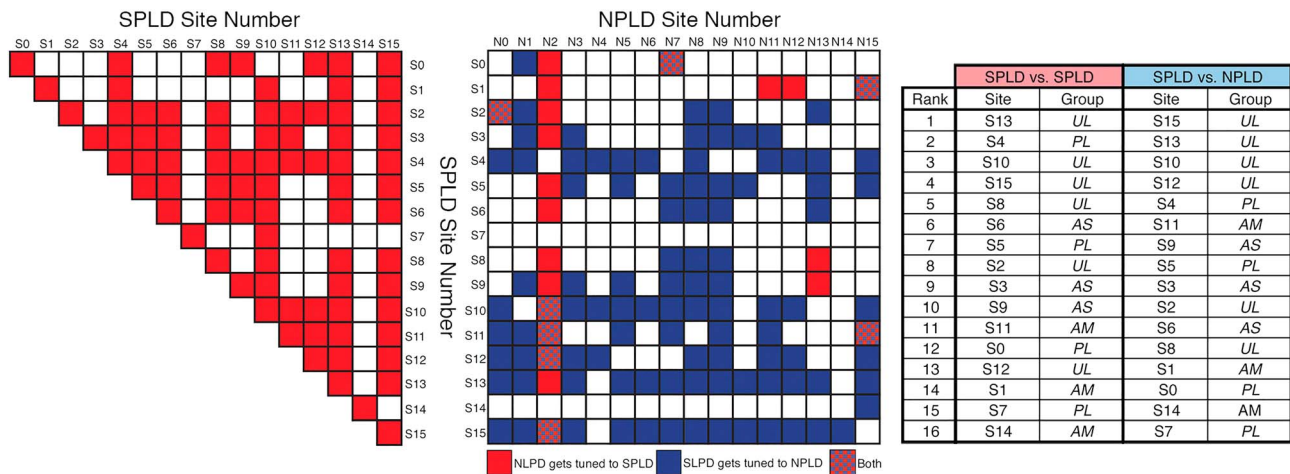


Figure 3. (left) Combinations of dynamic time warping tunings between South Polar Layered Deposits (SPLD) profiles that yield statistically significant matches (filled red squares). (center) Combinations of tunings of SPLD to North Polar Layered Deposits (NPLD) profiles that yield statistically significant matches. Filled blue squares represent good matches when the NPLD profile was kept fixed while the SPLD profile was tuned (Figure S4). Filled red squares represent good matches with the inverse tuning. (right) Ranking of SPLD profiles by the number of significant matches they achieve with other SPLD profiles (SPLD vs. SPLD) and with NPLD profiles (SPLD vs. NPLD).

Thirteen out of the 16 sites (81%, Table S2) display dominant wavelengths in their protrusion profiles that meet our significance criteria, and nine (56%, Figure 2d) have overlapping wavelength pairs and thus an identifiable climate signal. In the Australe Mensa (AM) group, S11 is the only site that qualifies, with wavelengths of 37 ± 6 and 20 ± 4 m and a ratio between them of $R_M = 1.85 \pm 0.48$. The Australe Scopuli (AS) group has two profiles with overlapping wavelengths, with means of 16 ± 3 and 9 ± 1 m, for a ratio $R_S = 1.78 \pm 0.35$. In Promethei Lingula (PL), S5 is the only site with overlapping wavelengths, equal to 26 ± 3 and 11 ± 2 m with a ratio $R_P = 2.36 \pm 0.51$. Finally, in Ultima Lingula (UL), five sites qualify, with mean wavelengths of 36 ± 3 and 17 ± 2 m, for a ratio $R_U = 2.12 \pm 0.31$.

Given that protrusion is likely a better stratigraphic property for paleoclimate studies (Becerra et al., 2016, 2017), we present analysis of protrusion profiles as our nominal results, but analysis on profiles of local slope and brightness are included in Table S2.

The sites in PL and UL sample similar elevations in the SPLD and have similar average wavelengths and ratios different from those detected in the adjacent AS group, suggesting that PL and UL could be part of the same record. Both Lingulae are stratigraphically and morphologically similar regions of the SPLD, and past work has implied that they constitute one stratigraphic unit (Milkovich & Plaut, 2008; Whitten & Campbell, 2018). We therefore combine PL and UL into one group (hereinafter referred to as PUL group), for which the average dominant wavelengths are 35 ± 3 and 16 ± 2 m, with a ratio $R_{PU} = 2.19 \pm 0.33$.

3.2. DTW

We used DTW to evaluate the uniformity of signals within the SPLD, that is, whether sites within one group correlate better to each other or to other groups, and to compare the 16 SPLD profiles to the 16 NPLD profiles (Becerra et al., 2016, 2017), in order to reveal similarities between the forcing of the two PLDs. The left and center panels of Figure 3 show the individual comparisons between all profiles, and the tables on the right rank the profiles by how well they match all other profiles in the SPLD and all profiles in the NPLD. For example, profile S13 achieves good matches with all but one SPLD profile (S7; Figure 3, left) and two NPLD profiles (N4 and N14; Figure 3, center), so it is ranked first in SPLD versus SPLD and second in SPLD versus NPLD. We then rank the geographic groups by the total number of good matches achieved by profiles in that group. The columns labeled “Group” display the group to which each ranked site belongs and so show which groups achieved better fits on average. In the SPLD versus SPLD case, profiles in UL achieve good matches with each other and with PL profiles, and in the SPLD versus NPLD case, UL again achieves the highest number of good matches with the NPLD.

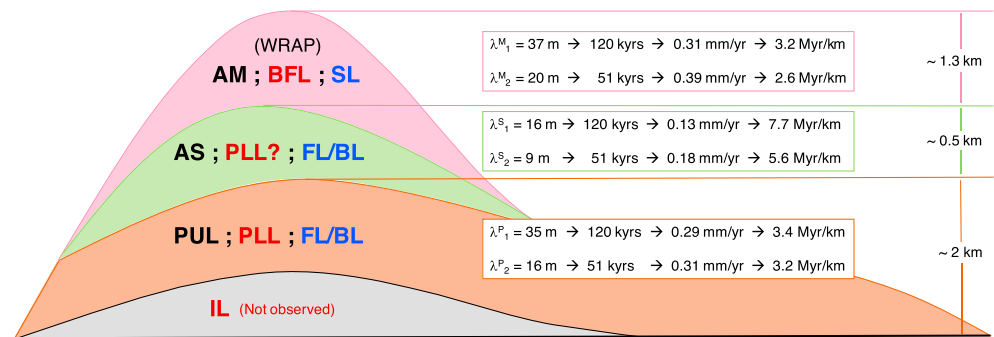


Figure 4. Schematic of stratigraphic units of the South Polar Layered Deposits and accumulation timescales. The abbreviated names of the units are on the left (see text). Black font = units defined here. Red font = sequences defined by Milkovich and Plaut (2008). Blue font = radar facies (Shallow (SL), Focused (FL), and Blurred (BL) Layer Facies) of Whitten and Campbell (2018). The lowermost inferred layer (IL) sequence (Milkovich & Plaut, 2008) was not observed here. Accumulation rates and times are shown on the right. AM = Austale Mensa; AS = Austale Scopuli; BFL = bench-forming layer; IL = inferred layer; PLL = Promethei Lingula layer; WRA = widespread recent accumulation package.

4. Discussion and Interpretation

4.1. Timescales of Accumulation

Insolation at Mars has five principal periodicities due to oscillations of various orbital parameters (Laskar et al., 2004). The WPS of the last 20 Myr of mean annual insolation over the SPLD (Figure S5a) shows that the most important of these are the precession of Mars' argument of perihelion (51 kyr) and the primary mode of oscillation of the obliquity (120 kyr), which have a ratio of 2.35. The emplacement of the SPLD likely occurred before 20 Ma, and the orbital solutions of Laskar et al. (2004) become chaotic further into the past. However, the change in the main oscillation frequencies over longer times is small enough that we can assume the same frequencies have forced the evolution of the insolation throughout at least the Late Amazonian, despite the solutions beyond 20 Ma being nonunique (Bills & Keane, 2019; Laskar et al., 2004). This stability is shown in Figures S5b and S5c, which show the spectral analysis of two insolation solutions with widely different behaviors over the past 250 Myr.

The detection of pairs of periodicities in the stratigraphy allows a comparison between their ratios and that of the insolation periods. Intuitively, if the ratios agree, each of the stratigraphic wavelengths can be related to the orbital periodicities to calculate average accumulation rates and time spans. However, stratigraphic ratios in the NPLD were found to be lower than the insolation forcing ratio by as much as 30% (Becerra et al., 2017). Models of the NPLD accumulation (Becerra et al., 2017; Hvidberg et al., 2012) showed that such lower ratios are consistent with orbital forcing if the relationship between ice accumulation and insolation is nonlinear. The similarities seen here between the average wavelengths and ratios of the SPLD and those in the NPLD (Becerra et al., 2017), as well as the results of the DTW comparison, show that it is reasonable to assume that the nature of the orbital forcing of the SPLD is similar to that of the NPLD. We thus interpret the stratigraphy as being consistent with orbital forcing if it contains statistically significant periodicities with ratios equal to, or smaller by at most 30% than, that in the insolation.

Our results indicate that at least three records of accumulation with distinct spectral characteristics are observed (Figure 4), in agreement with prior work (Milkovich & Plaut, 2008; Whitten et al., 2017; Whitten & Campbell, 2018). The lowermost record is in PUL. This record is overlain by a unit in AS, which is itself overlain by the topmost record in AM. The possible correlation with previously identified units is indicated in Figure 4.

Comparing the main insolation frequencies with the stratigraphic wavelengths allows us to estimate time-averaged limits on the accumulation rates of the different SPLD units. These are presented in Figure 4, where the long wavelength is tied to the 120-kyr period and the short to the 51-kyr period. For PUL, the accumulation rate derived from the 35- and 16-m wavelengths is 0.29–0.31 mm/year. The wavelengths of 16 and 9 m observed in AS profiles imply a decrease in accumulation rate to 0.13–0.18 mm/year, and AM wavelengths of 20 and 37 m signify an increase back to 0.31–0.39 mm/year.

We can then generate an order-of-magnitude estimate on the accumulation time by assuming a constant, geographically uniform accumulation rate throughout the entire SPLD, and no long periods of net ablation. If we assume the fastest accumulation rate of 0.39 mm/year—that of AM—to be valid for the whole SPLD stack, then it would have taken ~ 9.7 Myr to accumulate the 3.8 km (Plaut et al., 2007) of SPLD material. If we instead consider the slowest accumulation rate of 0.13 mm/year—that of AS—then the time to accumulate 3.8 km is ~ 28.5 Myr.

More detailed approximations of accumulation times for each unit can be calculated using thickness estimates from prior work (Milkovich & Plaut, 2008; Plaut et al., 2007; Whitten & Campbell, 2018) and absolute elevations in the DTMs. PUL exposures are located in a region of the SPLD between 0.5 and 2 km thick (Plaut et al., 2007). In AS, this thickness is 2.5–3.0 km (Plaut et al., 2007). Whitten et al. (2017) inferred that the PLL sequence (Milkovich & Plaut, 2008) must have had higher accumulation rates than the subsequent depositional periods. This agrees with the decrease in accumulation rate that we measure between PUL and AS. However, the PLL sequence appears to include both our PUL and AS units, making it difficult to define a boundary between them and thus a thickness for AS. We estimate this thickness from the elevation ranges of our profiles. In AS, the difference between the top of the highest-reaching valid profile (S6) and the bottom of the lowest-reaching valid profile (S9) is 570 m. In addition, the bottom of S9 barely overlaps with the top of S8, which is the highest-reaching valid profile in PUL (see profiles in Figure S2 for absolute elevations). We therefore assume that the AS unit must span at least ~ 500 m, and if up to 2 km of material corresponds to PUL, then 0.5–1 km must correspond to AS. The profiles in AM are located at the top of the thickest part of the SPLD, where the whole cap reaches thicknesses of 3.8 km. Subtracting the 2.5 to 3 km of PUL + AS leaves 0.8–1.3 km of material that could correspond to the AM record and overlie PUL and AS. This topmost record in AM could correspond to the BFL Sequence of Milkovich and Plaut (2008) and must also include the WRAP of Smith et al. (2016), although it cannot correspond exactly to it because the WRAP is stratigraphically above the BFL and is < 210 m thick, while the S11 profile in AM is > 500 m thick (see Figure S2.11).

Figure 4 displays our derived stratigraphic structure with accumulation times, as well as approximate comparisons with the units from previous work. We show the minimum estimated accumulation time for the SPLD, that is, the “faster” case in which AS is 0.5 km thick and AM is 1.3 km thick. Were it the case that the AM record is less than 1.3 km thick, the difference would be part of the AS record. With the derived rates, the 2-km stack in PUL would have accumulated in 6.4–6.9 Myr; the 0.5 km of AS would have been deposited in 2.8–3.9 Myr and the 1.3 km in AM in 3.4–4.2 Myr. These times combine to give a total accumulation time for the entire SPLD between 12.6 and 15 Myr.

Naturally, all estimates above are lower limits due to the assumption of no long hiatuses or periods of net ablation. The widespread presence of unconformities (Smith et al., 2016; Whitten & Campbell, 2018) are evidence that this is not the case. Still, our results show that a record of astronomically forced climate is present in the SPLD, although it is more complex than its counterpart in the NPLD.

Absolute dating of the SPLD requires a reliable age for a bed. The best estimates of surface age can be used to transform the time spans calculated here to ages of SPLD emplacement, resulting in a widest lower limit range for the onset of accumulation between ~ 17 Ma (considering the youngest 7-Ma age estimate of Herkenhoff, & Plaut 2000) and ~ 130 Ma (considering the oldest 100-Ma estimate of Koutnik et al., 2002). If the younger age is accurate, then the accumulation could potentially be modeled using the insolation solutions (Laskar et al., 2004), inviting research into a full-scale, paleoclimate-based accumulation model for both PLDs.

4.2. Uniformity and Comparison With the NPLD

The main implication derived from the DTW results is that the most uniform record is in UL and that profiles there correlate well with PL profiles, in agreement with the wavelet measurements and with the radar results that find neatly stacked beds in UL and PL (Whitten & Campbell, 2018). This also supports the idea that PUL as a whole represents a distinct record of accumulation (Milkovich & Plaut, 2008; Whitten et al., 2017; Whitten & Campbell, 2018). The comparison between other groups, however, is more ambiguous and gives no definitive implications that a particular record is observed within two sites of the same group. This complexity of the records outside UL could partially be explained by differential erosion or modification of the exposures. On the other hand, the uniformity of the UL record suggests that it may be the best place to

continue paleoclimate analysis, and the good matches between UL and NPLD profiles support the notion that regional climates in the south and north polar regions of Mars are influenced by the same factors, albeit at different times.

This relationship between the SPLD and the NPLD is also observed in the results of the wavelet analysis of the previous section (see Figure 2 here and Table 1 of Becerra et al., 2017). First, the mean wavelength ratios of all SPLD groups are within the uncertainty of the NPLD mean wavelength ratio. Second, the NPLD wavelengths themselves are similar to those detected in PUL. Lastly, the insolation periodicities inferred to have forced NPLD accumulation (Becerra et al., 2017) are the same ones that we infer to have forced SPLD accumulation.

5. Conclusions

Wavelet analysis of high-resolution stereo data of SPLD bed exposures has revealed the presence of statistically significant signals of climate forcing in the stratigraphic record, resulting in the calculation of accumulation rates for the SPLD of 0.13–0.39 mm/year and lower limits on the accumulation time between ~10 and ~30 Myr. The dominant stratigraphic periodicities vary according to geographic and stratigraphic location and indicate at least three periods of accumulation separated by changes in accumulation rate but forced by the same insolation periodicities. Signal matching shows that the most uniform record is in UL, making it the best place to continue paleoclimate analysis taking advantage of the capabilities of the CaSSIS instrument.

The stratigraphic record in the SPLD is more complex than that in the NPLD, but we have shown that a potentially readable record of astronomically forced climate is not only present there but also appears to have been forced by the same oscillations as its northern counterpart, hinting at a climatic connection between both ice sheets that spans tens of millions of years.

References

- Becerra, P., Byrne, S., Sori, M. M., Sutton, S., & Herkenhoff, K. E. (2016). Stratigraphy of the north polar layered deposits of Mars from high-resolution topography. *Journal of Geophysical Research: Planets*, 121, 1–27. [https://doi.org/10.1002/\(ISSN\)2169-9100](https://doi.org/10.1002/(ISSN)2169-9100)
- Becerra, P., Sori, M. M., & Byrne, S. (2017). Signals of astronomical climate forcing in the exposure topography of the North Polar Layered Deposits of Mars. *Geophysical Research Letters*, 44, 62–70. <https://doi.org/10.1002/2016GL071197>
- Bills, B. G., & Keane, J. T. (2019). Mars obliquity variations are both non-chaotic and possibly fully damped, *50th LPSC*, 1–2.
- Brown, A. J., Calvin, W. M., Becerra, P., & Byrne, S. (2016). Martian north polar cap summer water cycle. *Icarus*, 277, 401–415. <https://doi.org/10.1016/j.icarus.2016.05.007>
- Byrne, S., & Ivanov, A. B. (2004). Internal structure of the Martian south polar layered deposits. *Journal of Geophysical Research*, 109(E11001), 43–20. <https://doi.org/10.1029/2004JE002267>
- Cutts, J. A. (1973). Nature and origin of layered deposits of the Martian polar regions. *Journal of Geophysical Research, Planets*, 78(20), 4231–4249. <https://doi.org/10.1029/JB078i020p04231>
- Cutts, J. A., Blasius, K. R., Briggs, G. A., Carr, M. H., Greeley, R., & Masursky, H. (1976). North polar region of Mars: Imaging results from Viking 2. *Science*, 194(4271), 1329–1337. <https://doi.org/10.1126/science.194.4271.1329>
- Cutts, J. A., & Lewis, B. H. (1982). Models of climate cycles recorded in Martian polar layered deposits. *Icarus*, 50(2-3), 216–244. [https://doi.org/10.1016/0019-1035\(82\)90124-5](https://doi.org/10.1016/0019-1035(82)90124-5)
- Fishbaugh, K. E., & Hvidberg, C. S. (2006). Martian north polar layered deposits stratigraphy: Implications for accumulation rates and flow. *Journal of Geophysical Research*, 111(E6), E06012. <https://doi.org/10.1029/2005JE002571>
- Fishbaugh, K. E., Hvidberg, C. S., Byrne, S., Russell, P. S., Herkenhoff, K. E., Winstrup, M., & Kirk, R. (2010). First high-resolution stratigraphic column of the Martian north polar layered deposits. *Geophysical Research Letters*, 37, L07201. <https://doi.org/10.1029/2009GL041642>
- Hays, J. D., Imbrie, J., & Shackleton, N. J. (1976). Variations in the Earth's orbit: Pacemaker of the Ice Ages. *Science*, 194(4270), 1121–1132. <https://doi.org/10.2307/1743620?ref=search-gateway:5caad90dbd80f7c3ace71fec4f27a2aa>
- Herkenhoff, K., & Plaut, J. J. (2000). Surface ages and resurfacing rates of the polar layered deposits on Mars. *Icarus*, 144(2), 243–253. <https://doi.org/10.1006/icar.1999.6287>
- Herkenhoff, K. E., Byrne, S., Russell, P. S., Fishbaugh, K. E., & McEwen, A. S. (2007). Meter-scale morphology of the north polar region of Mars. *Science*, 317(5845), 1711–1715. <https://doi.org/10.1126/science.1143544>
- Howard, A. D., Cutts, J. A., & Blasius, K. R. (1982). Stratigraphic relationships within Martian polar cap deposits. *Icarus*, 50(2-3), 161–215. [https://doi.org/10.1016/0019-1035\(82\)90123-3](https://doi.org/10.1016/0019-1035(82)90123-3)
- Hvidberg, C. S., Fishbaugh, K. E., Winstrup, M., Svensson, A., Byrne, S., & Herkenhoff, K. E. (2012). Reading the climate record of the Martian polar layered deposits. *Icarus*, 221(1), 405–419. <https://doi.org/10.1016/j.icarus.2012.08.009>
- Kirk, R. L., Howington-Kraus, E., Rosiek, M. R., Anderson, J. A., Archinal, B. A., Becker, K. J., et al. (2008). Ultrahigh resolution topographic mapping of Mars with MRO HiRISE stereo images: Meter-scale slopes of candidate Phoenix landing sites. *Journal of Geophysical Research*, 113(E12), E00A03. <https://doi.org/10.1029/2007JE003000>
- Koutnik, M., Byrne, S., & Murray, B. (2002). South Polar Layered Deposits of Mars: The cratering record. *Journal of Geophysical Research, Planets*, 107(E11), 10–1–10–10. <https://doi.org/10.1029/2001JE001805>

Acknowledgments

The authors thank all the members and affiliates of the MRO/HiRISE and TGO/CaSSIS Science and Operation teams for their invaluable roles in acquiring and processing the data used in our study. The HiRISE data are available in the NASA Planetary Data System (pds.nasa.gov). The complete CaSSIS data set will be publicly available following successful review by ESA, foreseen for the third quarter of 2019 with release through ESA's Planetary Science Archive (PSA) thereafter. However, the CaSSIS DTM and corresponding stereo pair used in this study are available at <https://data.mendeley.com/datasets/nzwbhdsbch/draft?m=e52af18e-c9d9-40e6-8d3f-69bd3a964011>. We thank Christine Akers and Riley McClurkin for their efforts in producing the HiRISE DTMs, Miguel Almeida and Matthew Read for leading uplink and downlink of the CaSSIS data, and Cristina Re for her involvement in the CaSSIS DTM generation. We also especially thank Shane Byrne for his constructive comments before submission and Jennifer Whitten and Anna Grau Galofre for helpful reviews that greatly improved the manuscript. HiRISE science operations and DTM production facilities are headquartered in the HiRISE Operations Center (HiROC) of the Lunar and Planetary Laboratory (LPL, University of Arizona). CaSSIS is a project of the University of Bern and funded through the Swiss Space Office via ESA's PRODEX program. The instrument hardware development was also supported by the Italian Space Agency (ASI), INAF/Astronomical Observatory of Padova (ASI-INAF agreement 2017-03-17), and the Space Research Center (CBK) in Warsaw. Support from SGF (Budapest), LPL, and NASA Grant 80NSSC17K0510 (Sori) are also gratefully acknowledged. The wavelet software was written by C. Torrence and G. Compo and is available at <http://paos.colorado.edu/research/wavelets/>.

- Lalic, D. E., & Holt, J. W. (2017). New Martian climate constraints from radar reflectivity within the North Polar Layered Deposits. *Geophysical Research Letters*, 44, 657–664. <https://doi.org/10.1002/2016GL071323>
- Landis, M. E., Byrne, S., Daubar, I. J., Herkenhoff, K. E., & Dundas, C. M. (2016). A revised surface age for the North Polar Layered Deposits of Mars. *Geophysical Research Letters*, 43, 3060–3068. <https://doi.org/10.1002/2016GL068434>
- Laskar, J., Correia, A. C. M., Gastineau, M., Joutel, F., Levrard, B., & Robutel, P. (2004). Long term evolution and chaotic diffusion of the insolation quantities of Mars. *Icarus*, 170(2), 343–364. <https://doi.org/10.1016/j.icarus.2004.04.005>
- Laskar, J., Levrard, B., & Mustard, J. F. (2002). Orbital forcing of the Martian polar layered deposits. *Nature*, 419(6905), 375–377. <https://doi.org/10.1038/nature01066>
- Levrard, B., Forget, F., Montmessin, F., & Laskar, J. (2007). Recent formation and evolution of northern Martian polar layered deposits as inferred from a global climate model. *Journal of Geophysical Research*, 112(E6), E06012. <https://doi.org/10.1029/2006JE002772>
- Lewis, K. W., & Aharonson, O. (2014). Occurrence and origin of rhythmic sedimentary rocks on Mars. *Journal of Geophysical Research: Planets*, 119, 1432–1457. <https://doi.org/10.1002/2013JE004404>
- Lewis, K. W., Aharonson, O., Grotzinger, J. P., Kirk, R. L., McEwen, A. S., & Suer, T.-A. (2008). Quasi-periodic bedding in the sedimentary rock record of Mars. *Science*, 322(5907), 1532–1535. <https://doi.org/10.1126/science.1161870>
- Limaye, A. B. S., Aharonson, O., & Perron, J. T. (2012). Detailed stratigraphy and bed thickness of the Mars north and south polar layered deposits. *Journal of Geophysical Research*, 117(E6), E06009. <https://doi.org/10.1029/2011JE003961>
- Mann, M. E., & Lees, J. M. (1996). Robust estimation of background noise and signal detection in climatic time series. *Climatic Change*, 33(3), 409–445. <https://doi.org/10.1007/BF00142586>
- McEwen, A. S., Eliason, E. M., Bergstrom, J. W., Bridges, N. T., Hansen, C. J., Delamere, W. A., et al. (2007). Mars Reconnaissance Orbiter's High Resolution Imaging Science Experiment (HiRISE). *Journal of Geophysical Research*, 112(E5), 8048–8040. <https://doi.org/10.1029/2005JE002605>
- Milkovich, S. M. (2005). North polar cap of Mars: Polar layered deposit characterization and identification of a fundamental climate signal. *Journal of Geophysical Research*, 110(E1), 140–121. <https://doi.org/10.1029/2004JE002349>
- Milkovich, S. M., & Plaut, J. J. (2008). Martian South Polar Layered Deposit stratigraphy and implications for accumulation history. *Journal of Geophysical Research*, 113, E06007. <https://doi.org/10.1029/2007JE002987>
- Murray, B. C., Ward, W. R., & Yeung, S. C. (1973). Periodic insolation variations on Mars. *Science*, 180(4086), 638–640. <https://doi.org/10.2307/1736203?ref=search-gateway:2616173dedc2ffb87c104ea1bed2fe01>
- Perron, J. T., & Huybers, P. (2009). Is there an orbital signal in the polar layered deposits on Mars? *Geology*, 37(2), 155–158. <https://doi.org/10.1130/G25143A.1>
- Phillips, R. J., Zuber, M. T., Smrekar, S. E., Mellon, M. T., Head, J. W., Tanaka, K. L., et al. (2008). Mars north polar deposits: Stratigraphy, age, and geodynamical response. *Science*, 320(5880), 1182–1185. <https://doi.org/10.1126/science.1157546>
- Plaut, J. J., Picardi, G., Safaeinili, A., Ivanov, A. B., Milkovich, S. M., Cicchetti, A., et al. (2007). Subsurface radar sounding of the South Polar Layered Deposits of Mars. *Science*, 316(5821), 92–95. <https://doi.org/10.1126/science.1139672>
- Putzig, N. E., Phillips, R. J., Campbell, B. A., Holt, J. W., Plaut, J. J., Carter, L. M., et al. (2009). Subsurface structure of Planum Boreum from Mars Reconnaissance Orbiter Shallow Radar soundings. *Icarus*, 204(2), 443–457. <https://doi.org/10.1016/j.icarus.2009.07.034>
- Seu, R., Phillips, R. J., Biccari, D., Orosei, R., Masdea, A., Picardi, G., et al. (2007). SHARAD sounding radar on the Mars Reconnaissance Orbiter. *Journal of Geophysical Research*, 112(E5), E05S05. <https://doi.org/10.1029/2006JE002745>
- Simioni, E., Re, C., Mudric, T., Pommerol, A., Thomas, N., & Cremonese, G. (2017). A Photogrammetric pipeline for the 3D reconstruction of CaSSIS images on board ExoMars TGO. *International Archives of the Photogrammetry, Remote Sensing and Spatial Information Science*, XLII-3/W1, 133–139. <https://doi.org/10.5194/isprs-archives-XLII-3-W1-133-2017>
- Smith, I. B., Diniega, S., Beaty, D. W., Thorsteinsson, T., Becerra, P., Bramson, A. M., et al. (2017). 6th international conference on Mars polar science and exploration: Conference summary and five top questions. *Icarus*, 308, 2–14. <https://doi.org/10.1016/j.icarus.2017.06.027>
- Smith, I. B., Putzig, N. E., Holt, J. W., & Phillips, R. J. (2016). An ice age recorded in the polar deposits of Mars. *Science*, 352(6289), 1075–1078. <https://doi.org/10.1126/science.aad6968>
- Sori, M. M., Perron, J. T., Huybers, P., & Aharonson, O. (2014). A procedure for testing the significance of orbital tuning of the Martian polar layered deposits. *Icarus*, 235(C), 136–146. <https://doi.org/10.1016/j.icarus.2014.03.009>
- Thomas, N., Cremonese, G., Ziethe, R., Gerber, M., Brändli, M., Bruno, G., et al. (2017). The Colour and Stereo Surface Imaging System (CaSSIS) for the ExoMars Trace Gas Orbiter. *Space Science Reviews*, 212(3–4), 1897–1944. <https://doi.org/10.1007/s11214-017-0421-1>
- Toon, O. B., Pollack, J. B., Ward, W., Burns, J. A., & Bilski, K. (1980). The astronomical theory of climatic-change on Mars. *Icarus*, 44(3), 552–607. [https://doi.org/10.1016/0019-1035\(80\)90130-X](https://doi.org/10.1016/0019-1035(80)90130-X)
- Torrence, C., & Compo, G. P. (1998). A practical guide to wavelet analysis. *Bulletin of the American Meteorological Society*, 79(1), 61–78. [https://doi.org/10.1175/1520-0477\(1998\)079<0061:APGTWA>2.0.CO;2](https://doi.org/10.1175/1520-0477(1998)079<0061:APGTWA>2.0.CO;2)
- Whitten, J. L., & Campbell, B. A. (2018). Lateral continuity of layering in the Mars South Polar Layered Deposits from SHARAD sounding data. *Journal of Geophysical Research: Planets*, 123(6), 1541–1554. <https://doi.org/10.1029/2018JE005578>
- Whitten, J. L., Campbell, B. A., & Morgan, G. A. (2017). A subsurface depocenter in the South Polar Layered Deposits of Mars. *Geophysical Research Letters*, 44, 8188–8195. <https://doi.org/10.1002/2017GL074069>

References From the Supporting Information

- Acton, C., Bachman, N., Semenov, B., & Wright, E. (2018). A look towards the future in the handling of space science mission geometry. *Planetary and Space Science*, 150, 9–12. <https://doi.org/10.1016/j.pss.2017.02.013>
- Acton, C. H. Jr. (1996). Ancillary data services of NASA's Navigation and Ancillary Information Facility. *Planetary and Space Science*, 44(1), 65–70. [https://doi.org/10.1016/0032-0633\(95\)00107-7](https://doi.org/10.1016/0032-0633(95)00107-7)
- Briechele, K., & Hanebeck, U. D. (2001). Template matching using fast normalized cross correlation. *Proc. SPIE 4387, Optical Pattern Recognition XII*. <https://doi.org/10.1117/12.421129>
- Farge, M. (1992). Wavelet transforms and their applications to turbulence. *Annual Review of Fluid Mechanics*, 24(1), 395–458. <https://doi.org/10.1146/annurev.fl.24.010192.002143>
- Gruen, A. (1985). Adaptive least squares correlation: A powerful image matching technique. *South African Journal of Photogrammetry, Remote Sensing and Cartography*, 14, 175–187.

- Haam, E., & Huybers, P. (2010). A test for the presence of covariance between time-uncertain series of data with application to the Dongge Cave speleothem and atmospheric radiocarbon records. *Paleoceanography*, 25, PA2209. <https://doi.org/10.1029/2008PA001713>
- Re, C., Roncella, R., Forlani, G., Cremonese, G., & Naletto, G. (2014). Evaluation of an Area-Based matching algorithm with advanced shape models. *International Archives of the Photogrammetry, Remote Sensing and Spatial Information Science*, XL-4, 215–221. <https://doi.org/10.5194/isprsarchives-XL-4-215-2014>
- Shean, D. E., Alexandrov, O., Moratto, Z. M., Smith, B. E., Joughin, I. R., Porter, C., & Morin, P. (2016). An automated, open-source pipeline for mass production of digital elevation models (DEMs) from very-high-resolution commercial stereo satellite imagery. *ISPRS Journal of Photogrammetry and Remote Sensing*, 116, 101–117. <https://doi.org/10.1016/j.isprsjprs.2016.03.012>